CHAPTER 2

Gel electrolyte assisted Al^{3+} ion capacitor with electrospun MoO_3

Gel electrolyte assisted Al^{3+} ion capacitor with electrospun MoO_3

2.1 Introduction

As discussed in the introduction chapter, electrochemical capacitors or supercapacitors are the significant kind of electrochemical energy storage device. They show enormous promise because of their capacity to store energy and exhibit power densities similar to those of batteries and conventional capacitors [1-4]. Furthermore, electrochemical capacitors exhibit some of the most desirable characteristics. For example, the capability to sustain relatively long cycle life, work across wide temperature range, ability to fabricate in flexible, self healing [5-7]. Although the first Li^+ ion capacitor was reported in non-aqueous ($LiPF_6$/acetonitrile) electrolyte using $Li_4Ti_5O_{12}$ and activated as anode and as cathode respectively, but it could offer energy density of only 18 Wh kg^{-1} [8]. It was mentioned in the introduction chapter that lithium (Li) has the less abundance (~ 0.003 %) in the earth crust and has the environmental safety issues. Therefore, research work is gaining attention on other earth abundant electrochemically active ions such as K^+, Na^+, Mg^{2+}, Al^{3+} etc. [9]. Among these, utilization of Al^{3+} has the advantages over other ions such as three electron transfer per cation, smaller ionic radius, low cost, easy processing and storage at ambient atmosphere. Thalji et al. described the outcomes of Al^{3+} ion asymmetric supercapacitor by using $W_{18}O_{49}$ nanowire and reduced graphene oxide which shows specific capacitance about 350 Fg^{-1} at current density of 1 Ag^{-1} over 12,000 cycles [10]. Similarly, Li et al. studied the Al^{3+} ion storage behavior of an asymmetric capacitor by utilizing $W_{18}O_{49}$/SCNT and polyaniline/SCNT electrodes [11]. Ma et al. described an Al^{3+} ion capacitor based on graphene and MXene as electrodes [12]. It was also mentioned in the introduction chapter that electrolytes play an important role in the electrochemical capacitors because the potential window can vary in different electrolytes. In light of this, gel electrolyte can deliver wider potential window as compared with aqueous electrolyte [13-17]. MoO_3 is a technologically promising electrode material which has been investigated in various applications purposes such as energy storage, photovoltaics, electrochromic devices, catalysis, sensors etc. [18-24]. From the view point of multivalent guest ion insertion in an electrochemical reaction, Mo is important because of its variable oxidation states (-II to +VI) [25]. There are studies of MoO_3 being used as electrode material in

electrochemical capacitors [26-35]. However, Al^{3+} ion insertion studies in MoO_3 are very few [36, 37]. Keeping all the above discussed points in mind, the electrochemical performance of an electrochemical capacitor with MoO_3 nanorod is illustrated in this chapter.

2.2 Experimental Section

2.2.1 Materials

Polyvinyl alcohol (PVA) (M_w ~ 125,000, Sigma Aldrich), Ammonium molybdate tetrahydrate ($(NH_4)_6Mo_7O_{24}.4H_2O$, Rankem, Avantor Performance Materials India Ltd.), Graphite powder (Lobachemie Pvt. Ltd.), Ethanol and Polyvinylidene fluoride (PVDF) (Sigma Aldrich), Aluminium chloride anhydrous powder (Merck), Carbon black and N-methyl-2-pyrrolidone (Alfa aesar) and Distilled water.

2.2.2 Synthesis

2.2.2.1 *Synthesis of PVA/ammonium molybdate solution*

The synthesis process is adopted from ref [38]. First, 10 wt % PVA solution was made by dissolving 10 g of PVA in 90 ml of distilled water at 96 ^oC. After cooling the mixture to room temperature, 20 ml of PVA solution was slowly dropped in an ammonium molybdate tetrahydrate solution which is basically prepared by mixing 0.5 g of $(NH_4)_6Mo_7O_{24}.4H_2O$ in 2 ml ethanol and 2 ml distilled water. The overall mixture was stirred in a water bath at 60 ^oC for 5 h. Finally, a viscous PVA/ammonium molybdate composite solution was obtained which was further used for electrospinning.

2.2.2.2 Synthesis of reduced graphene oxide

At first, graphene oxide was prepared by using modified Hummer's method [39]. In a typical procedure, 1 g of graphite powder was pre-oxidized in 46 ml of concentrated H_2SO_4 along with 1 g of $NaNO_3$. Then the mixture was stirred in ice bath for 4 h. After that, 6 g of $KMnO_4$ was slowly added in to the mixture and stirred for 1 h at 35 ^oC. Then after cooling to room temperature, added 90 ml of distilled water and again stirred for 1 h. The mixture was then stirred for 2 h at around 90 ^oC and added 200 ml of distilled water. Later, 30 ml of 30 % H_2O_2 was added in the

mixture. The mixture was then washed with 200 ml of 5 % HCl solution and kept for 2 days to settle down. To remove the impurities, the mixture was then washed with distilled water for several times and collected by centrifugation. The material was dried at 60 ^{o}C for 10 h to obtain graphene oxide. The graphene oxide was exfoliated by dispersing 2 g of GO in 1000 ml distilled water and, subsequent ultrasonication for 2 h. The exfoliated GO was collected again by centrifugation. 400 mg of the prepared exfoliated GO was further dispersed in 800 ml of distilled water and continuously stirred at 95 ^{o}C for 4 days. Finally, the mixture was centrifuged and it dried at 60 ^{o}C to obtain rGO.

2.2.2.3 Synthesis of rGO/PVA/ammonium molybdate solution

2 mg of rGO was dispersed in already described PVA/ammonium molybdate solution (10 ml) by sonication for 1 h. The homogeneously rGO dispersed PVA/ammonium molybdate solution was used for further electrospinning.

2.2.2.4 Electrospinning of MoO_3 and rGO/MoO_3

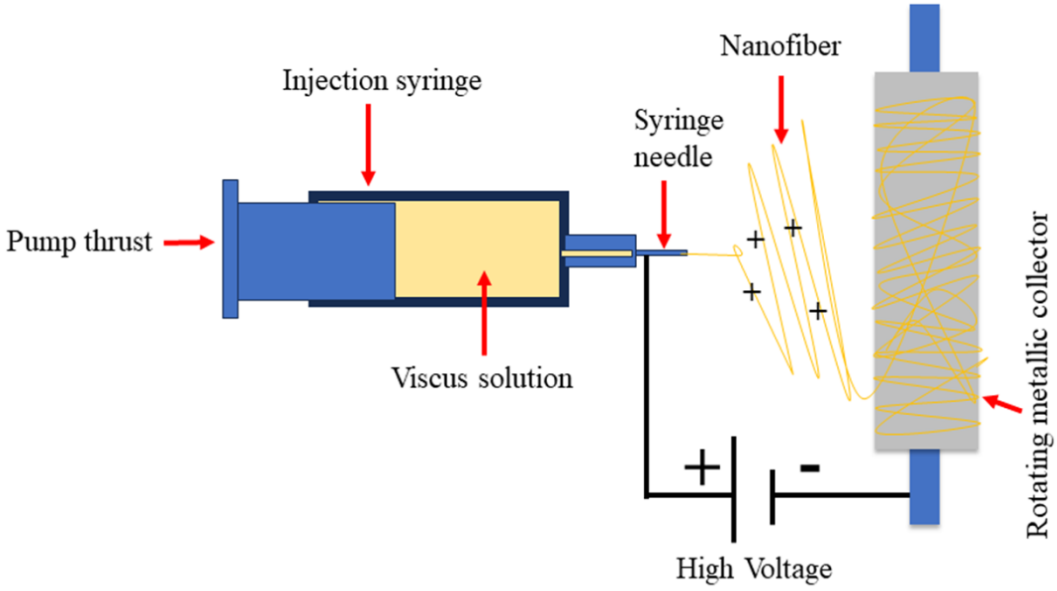

Figure 2.1: Schematic diagram of electrospinning setup.

As shown in the above schematic diagram, PVA/ammonium molybdate solution was loaded in a 3 ml plastic syringe and the flow of the solution was maintained at a constant flow rate (0.5 ml/h). A voltage of 20 kV was applied to the needle tip while performing. The distance between the tip of the needle and the material collector was 10 cm. The collector was covered with an aluminium foil. The material obtained after electrospinning was dried in oven at 70 ^{o}C for 10 h and finally

calcined at 500 ^{o}C for 3 h. PVA and $(NH_4)_6Mo_7O_{24}.4H_2O$ were used as the precursors for electrospinning. The reason for using PVA is because it is a highly water soluble polymer. On the other hand, $(NH_4)_6Mo_7O_{24}.4H_2O$ is the primary source of MoO_3. When heated above 300 ^{o}C, $(NH_4)_6Mo_7O_{24}.4H_2O$ decomposes to MoO_3 [40, 41]. In addition, it is also highly water soluble salt. Therefore, the synthesis can be performed avoiding organic solvents. rGO/MoO_3 was fabricated using the similar electrospinning process keeping the parameters constant as the pristine MoO_3. However, rGO/PVA/ammonium molybdate solution was loaded in to the syringe. The obtained material was further calcined at 500 ^{o}C for 3 h.

2.2.3 Characterizations

The structural properties were analyzed by powder X ray diffraction (BRUER AXS D8 FOCUS, Cu-$K_\alpha$radiation; $\lambda = 1.5406\dot{A}$) and Raman spectroscopy (RENISHAW BASIS SERIES WITH 515 LASER, RENISHAW, UK). The surface morphology was analyzed using scanning electron microscope (SEM, JEOL, 6390LV and ZEISS, SIGMA). The thermal analysis was performed by thermogravimetric analyser (TGA).

2.2.4 Electrochemical measurements

MoO_3 and rGO/MoO_3 obtained via electrospinning were used to fabricate the working electrode. MoO_3 or rGO/MoO_3, carbon black and polyvinylidene fluoride were mixed in 1-methyl -2 pyrrolidone (NMP) in 8:1:1 ratio to obtain a homogeneous slurry which was drop-coated onto a piece of graphite paper current collector. The electrodes were then dried at 120 ^{o}C for 12 h to evaporate the solvent. The corresponding active masses on each electrode were noted down. The electrochemical measurements were performed in aqueous 1 M $AlCl_3$ electrolyte and gel electrolyte (1 M $AlCl_3$-PVA). The gel electrolyte (1 M $AlCl_3$-PVA) was prepared by mixing 15 wt% of PVA in 1 M $AlCl_3$ aqueous electrolyte at 96 ^{o}C for 2 h. The digital photographs of the prepared aqueous and gel electrolytes are shown in (Figure 2.2a and 2.2b). For the three electrode electrochemical measurements, Ag/AgCl, Pt and MoO_3 were used as the reference, counter and working electrode respectively. For symmetric supercapacitor estimation, two electrode system with MoO_3 or rGO/MoO_3 electrodes were used. The symmetric supercapacitors are designated as MoO_3//MoO_3 and rGO/MoO_3//rGO/MoO_3. The active masses of both the electrodes were

maintained identical. The specific capacitance (C_s) was calculated using the equation: $C_s = \frac{2 \times I \times \Delta t}{m \times \Delta V}$ Fg^{-1}, where I is the applied current (in A), Δt is the discharge time (in s), m is the mass loaded on the single electrodes (in g), ΔV is the discharge potential interval (in V).

The energy (E) and power (P) density were calculated by using the following two equations (2.1) and (2.2) respectively.

$$E = \frac{1}{2} C_s (\Delta V)^2 \times \frac{1000}{3600} \quad Wh\ kg^{-1} \text{.....(2.1)}$$

$$P = \frac{E}{\Delta t} = \frac{I \times \Delta V}{2m} \times 1000 \quad W\ kg^{-1} \text{.....(2.2)}$$

where all the terms have usual meanings as mentioned in C_s.

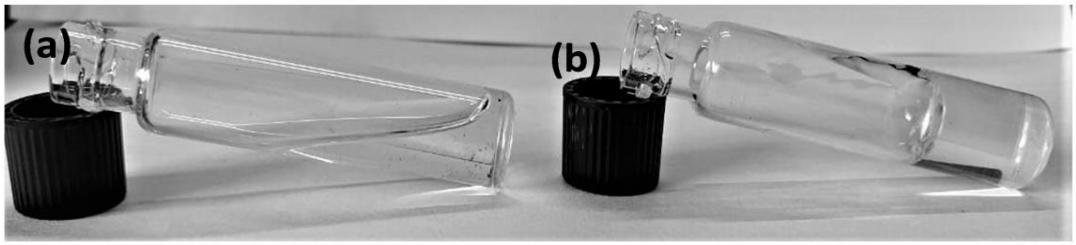

Figure 2.2: Digital photographs of (a) 1 M $AlCl_3$ aqueous electrolyte and (b) 1 M $AlCl_3$-PVA gel electrolyte.

2.3 Results and discussion

Figure 2.3 shows the XRD patterns of the as prepared PVA/ammonium molybdate nanofiber, MoO_3 and rGO/MoO_3 nanorods. A broad peak around $2\theta = 19^o$ corresponding to the (101) plane of PVA could be seen in PVA/ammonium molybdate nanofiber. After calcination, the PVA/ammonium molybdate nanofiber converts to crystalline MoO_3 nanorod. All the diffraction peaks could be identified as the pure orthorhombic phase of MoO_3 (α-MoO_3, JCPDS No. 05-0508) for MoO_3 nanorod and rGO/MoO_3 nanorod. No prominent diffraction peaks of rGO were seen due to trace amount of rGO in the composite. Thermogravimetric analysis confirms presence of ~ 2.13 wt% of rGO in the rGO/MoO_3 composite (Figure 2.4a). The estimation is done by considering the difference in the weight loss from 575 ^oC. The XRD patterns of graphene oxide (GO) as well as reduced graphene oxide (rGO) are shown in (Figure 2.4b) which match well with the reported literature [42]. Raman

spectra show peaks in the range 250–1050 cm^{-1} which are attributed to the stretching and bending of Mo-O bonds (Figure 2.5). These are identical to the previously reported data [43]. However, an additional small intensity peak around 1624 cm^{-1} was observed in rGO/MoO_3 which could be interpreted as the G band of rGO (inset of Figure 2.5).

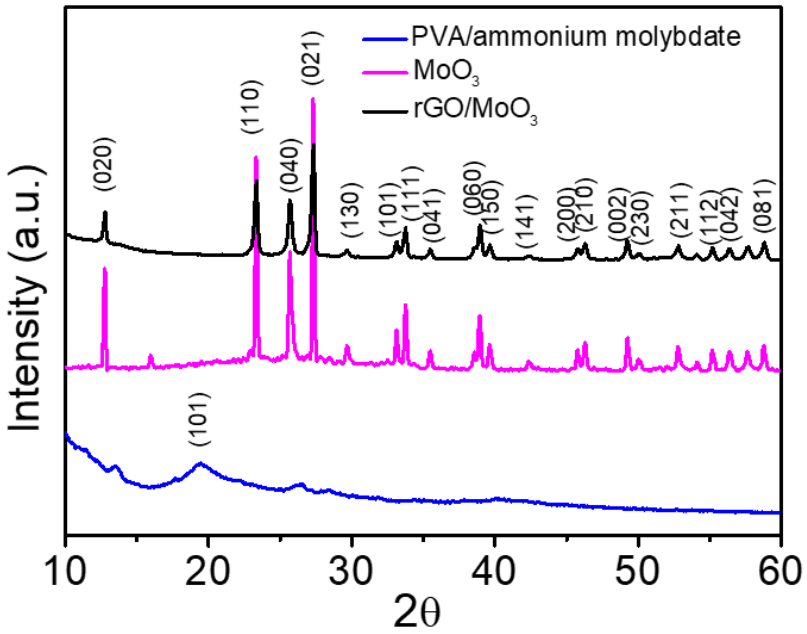

Figure 2.3: XRD patterns of PVA/ammonium molybdate composite nanofibers, MoO_3 and rGO/MoO_3 nanorods.

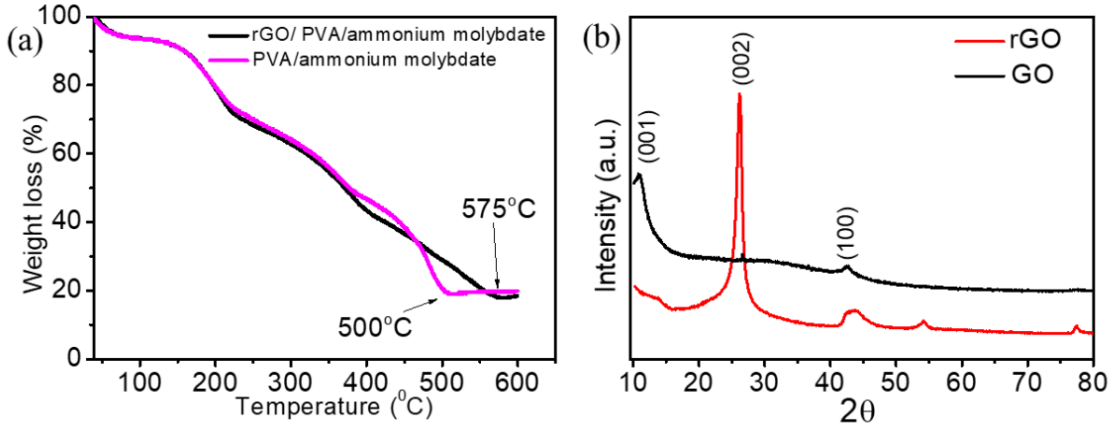

Figure 2.4: (a) Thermogravimetric analysis (TGA) curve of PVA/ammonium molybdate composite nanofibers and rGO/PVA/ammonium molybdate composite nanofibers and (b) XRD patterns of graphene oxide (GO) as well as reduced graphene oxide (rGO).

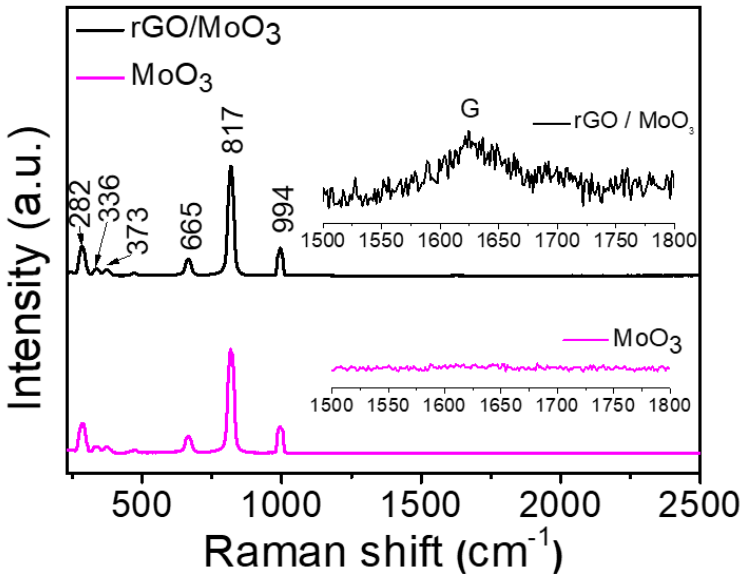

Figure 2.5: Raman spectra of MoO_3 and rGO/MoO_3 nanorods with inset views in the range of 1500 cm^{-1} to 1800 cm^{-1} to show the G band.

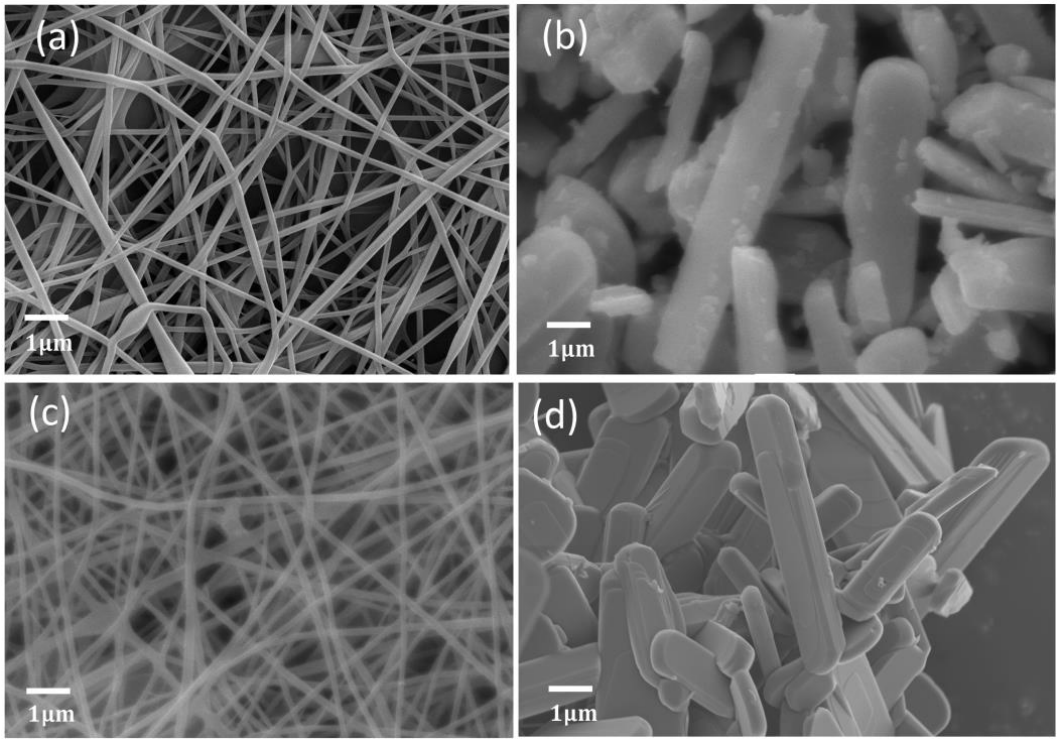

Figure 2.6: SEM images of (a) PVA/ammonium molybdate composite nanofibers, (b) MoO_3 nanorod after calcination, (c) rGO/PVA/ammonium molybdate composite nanofibers and (d) rGO/MoO_3 nanorod after calcination.

Figure 2.6a shows the SEM images of the prepared PVA/ammonium molybdate composite nanofibers, where it is seen that the nanofibers are uniformly

distributed. After calcination, the PVA/ammonium molybdate composite nanofibers turn into MoO_3 nanorod structure (Figure 2.6b). Similar structure could also be observed for rGO/PVA/ammonium molybdate composite nanofibers and rGO/MoO_3 (Figure 2.6c and 2.6d). The decomposition of PVA and ammonium molybdate and subsequent recrystallization of decomposed ammonium molybdate during the calcination process results in the structural change as was illustrated in an earlier study [38].

Figure 2.7a shows the CV profiles of MoO_3 in 1 M $AlCl_3$ aqueous electrolyte at scan rate (= 2.5 mVs^{-1}). It could be seen that the material shows prominent electrochemical activity. Three cathodic peaks named as A, B and C are noted at -0.33 V, -0.55 V and -0.80 V respectively. Subsequently, there exists three anodic peaks at -0.09 V, -0.51 V and -0.64 V which are labelled as $A^{/}$, $B^{/}$ and $C^{/}$respectively. This electrochemical activity is similar to the previously reported literature [36]. Similar electrochemical activity could also be seen for rGO/MoO_3 nanorod (Figure 2.7b). The electrochemical activity of rGO/MoO_3 nanorod was also investigated in the gel electrolyte (1 M $AlCl_3$-PVA) and the composite shows similar redox behaviors (Figure 2.7c). At present, we do not have direct evidence of the changes occurred during the electrochemical process. However, an analogy could be drawn from the known fact of Li^+ ion insertion in α-MoO_3 where multistep (mostly two-step) electrochemical reactions occur [44-46]. It is verified that Li^+ ion can intercalate between the weakly bound (vdW interaction) [MoO_6] octahedra interlayer and between [MoO_6] octahedra intralayer [44-46]. These two Li^+ ion intercalation processes result in two pairs of redox peaks. Again, it was also observed that the (020) diffraction peak of MoO_3 completely vanished with concomitant appearance of a new diffraction peak at around 11.42^o due to Li^+ ion intercalation [44]. Similar effect but with appearance of two additional diffraction peaks could also be noticed in the case of Al^{3+} ion insertion in MoO_3 as per previous study [36]. Therefore, it could be commented that the occurrence of three pairs of highly reversible cathodic and anodic redox peaks in the case of Al^{3+} ion insertion in MoO_3 suggests complicated multistep electrochemical reactions which may involve Al^{3+} ion intercalation in between [MoO_6] octahedra interlayer and inside [MoO_6] octahedra.

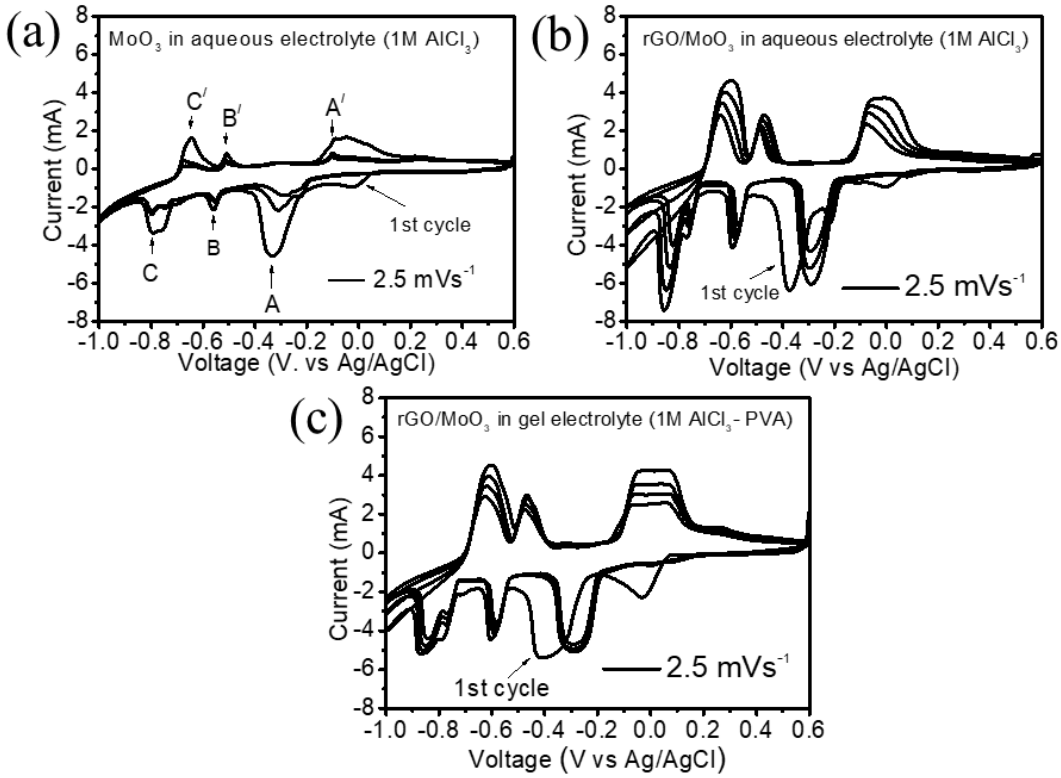

Figure 2.7: CV curves of (a) MoO_3 nanorod and (b) rGO/MoO_3 nanorod in 1 M $AlCl_3$ aqueous electrolyte, (c) rGO/MoO_3 in gel electrolyte (1 M $AlCl_3$-PVA).

Now, the CV experiments were conducted for MoO_3 nanorod in a symmetric electrochemical capacitor configuration in 1 M $AlCl_3$ aqueous electrolyte. The potential window of the MoO_3//MoO_3 symmetric cell was optimized by performing a series of CV experiments at a scan rate of 2 mVs^{-1}. The initial potential window was (0-1.3) V (Figure 2.8a). As could be seen, there are two redox peaks. The cathodic peak is at 0.44 V and the anodic peak is at 0.98 V. When the potential window was increased to 1.5 V (Figure 2.8b), the CV profile is different than the obtained CV profile in the voltage range of (0-1.3) V. There are now two prominent cathodic scan peaks at 0.07 V and 1.10 V. A broad peak could be seen around 0.66 V. Similarly, three anodic scan peaks at 0.24 V, 1.20 V and 1.43 V could be noticed. As could be verified from the CV profiles for the potential windows in the range (0-1.7) V (Figure 2.8c) and (0-1.9) V (Figure 2.8d), these profiles are almost identical to the profile obtained in the potential window of (0-1.5) V. Therefore, rest of the experiments were performed within this range. Experiments were also performed with rGO/MoO_3//rGO/MoO_3 symmetric cell and the characteristics of the CV profile (Figure 2.9(a-c)) in this case is almost similar to MoO_3//MoO_3 symmetric cell.

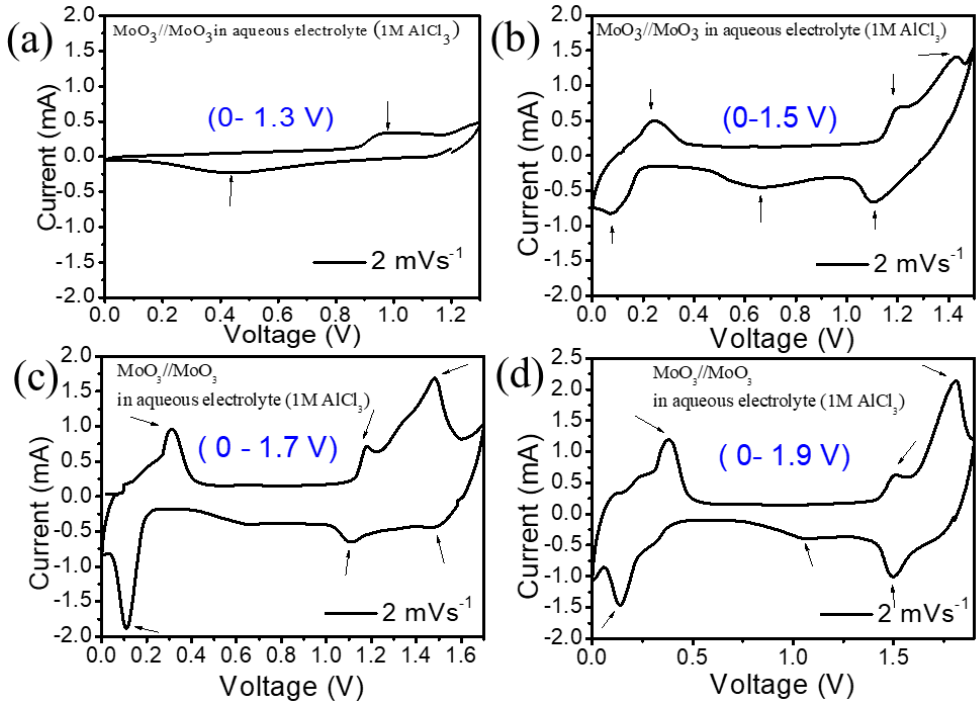

Figure 2.8: CV curves of MoO_3//MoO_3 symmetric cell in 1 M $AlCl_3$ aqueous electrolyte in the potential window of (a) (0-1.3) V and (b) (0-1.5) V, (c) (0-1.7) V and (d) (0-1.9) V.

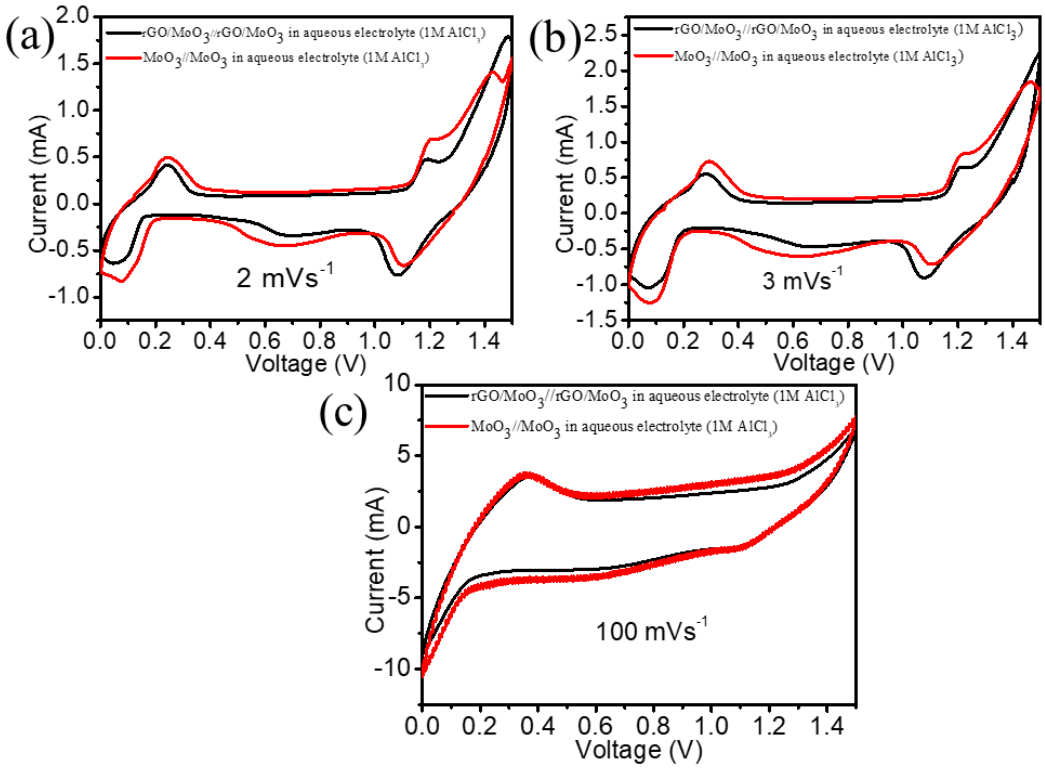

Figure 2.9: CV curves of MoO_3//MoO_3 and rGO/MoO_3//rGO/MoO_3 in the potential window of (0-1.5) V at scan rates of (a) 2 mVs^{-1}, (b) 3 mVs^{-1}, (c) 100 mVs^{-1} in 1 M $AlCl_3$ aqueous electrolyte.

Again, CV experiments were performed with the gel electrolyte for $rGO/MoO_3//rGO/MoO_3$ symmetric arrangement (Figure 2.10a). In this case, it could be noticed that the current response of the redox peaks at 0.07 V and 0.24 V is much higher than the redox peaks obtained in the (1-1.5) V region. This feature is in contrast to the CV profiles obtained in pristine aqueous electrolyte (Figure 2.8b). It is interesting to note here that when the potential window is increased to 2 V (Figure 2.10b), there is a shift of the low potential redox peaks by an amount of 0.4 V towards the positive side. Similar behavior could also be noticed for the potential window of (0-2.2) V (Figure 2.10c) except a sharp increase of current at higher potential region (~ 1.5-2.2 V). On the other hand, when the potential window is changed to (0-2.4) V, the obtained CV profile (Figure 2.10d) is quite different than the previous cases. Considering this point, further experiments with gel electrolyte were performed in the potential window of (0-2) V. Another striking feature is noticed at high scan rates. The CV profiles at high scan rates (for example at 100 mVs^{-1}) is of quasi-rectangular shape for both $MoO_3//MoO_3$ and $rGO/MoO_3//rGO/MoO_3$ cells in pristine aqueous electrolyte (Figure 2.11f and 2.12f). In contrast, quasi-rectangular feature could not be noticed in the gel electrolyte, rather peaks at 0.47 V and 1 V could be prominently visible (Figure 2.13f).

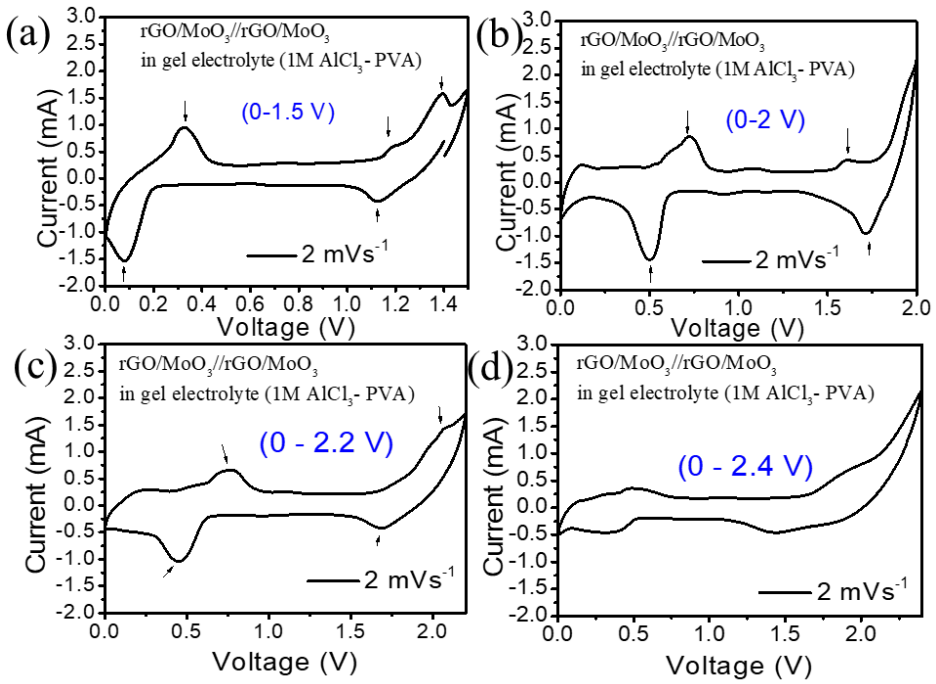

Figure 2.10: CV curves of $rGO/MoO_3//rGO/MoO_3$ symmetric cell in gel electrolyte (1 M $AlCl_3$-PVA) in the potential window of (a) (0-1.5) V, (b) (0-2) V, (c) (0-2.2) V and (d) (0-2.4) V. The scan rate is 2 mVs^{-1}.

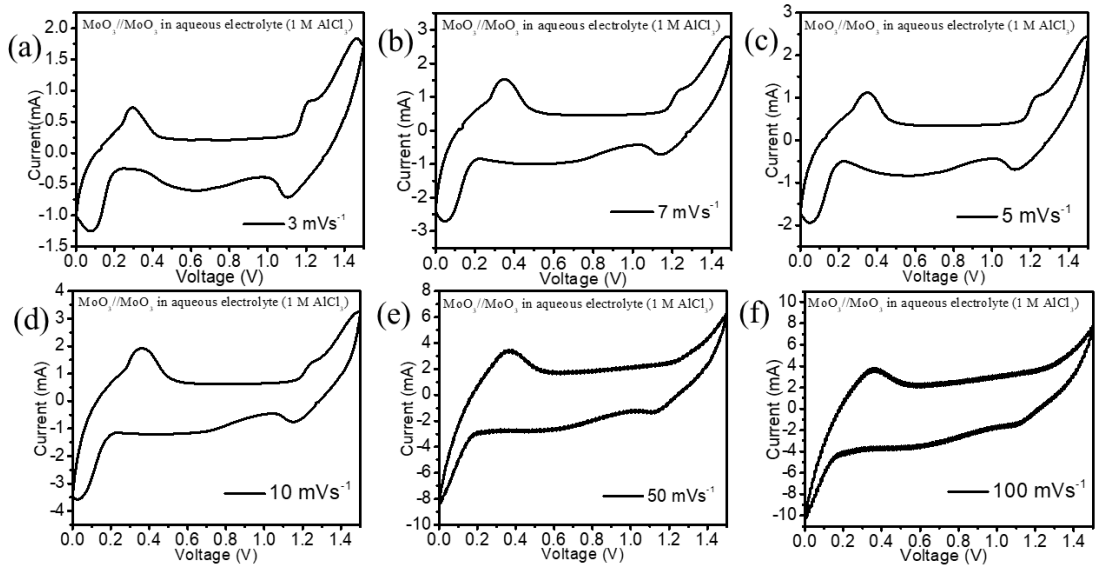

Figure 2.11: CV curves of MoO_3//MoO_3 cell in the potential range of (0-1.5) V at scan rate of (a) 3 mVs^{-1}, (b) 5 mVs^{-1}, (c) 7 mVs^{-1}, (d) 10 mVs^{-1}, (e) 50 mVs^{-1}, and (f) 100 mVs^{-1} in aqueous electrolyte (1 M $AlCl_3$).

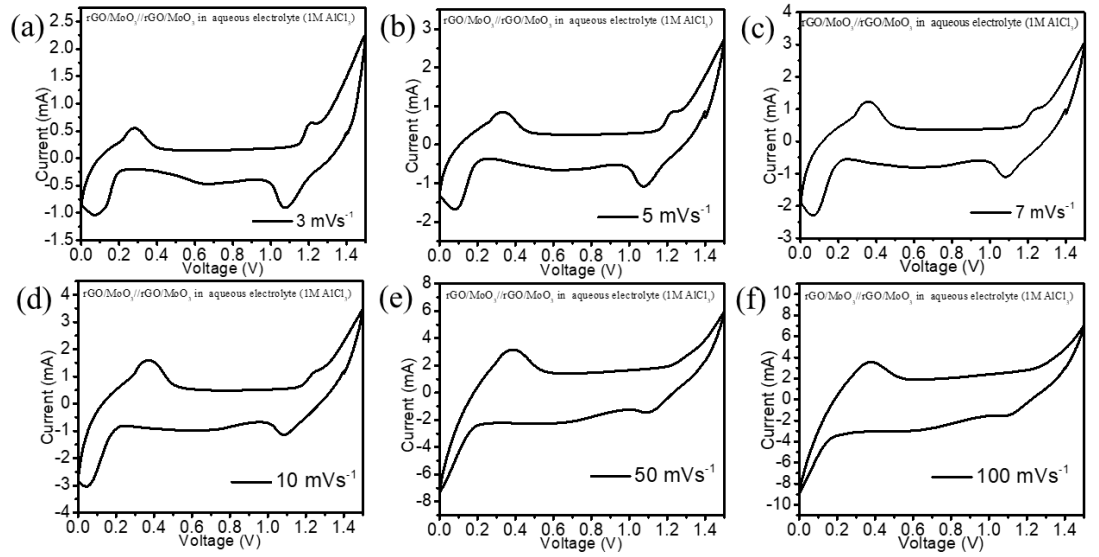

Figure 2.12: CV curves of rGO/MoO_3//rGO/MoO_3 cell in the potential range of (0-1.5) V at scan rate of (a) 3 mVs^{-1}, (b) 5 mVs^{-1}, (c) 7 mVs^{-1}, (d) 10 mVs^{-1}, (e) 50 mVs^{-1}, and (f) 100 mVs^{-1} in aqueous electrolyte (1 M $AlCl_3$).

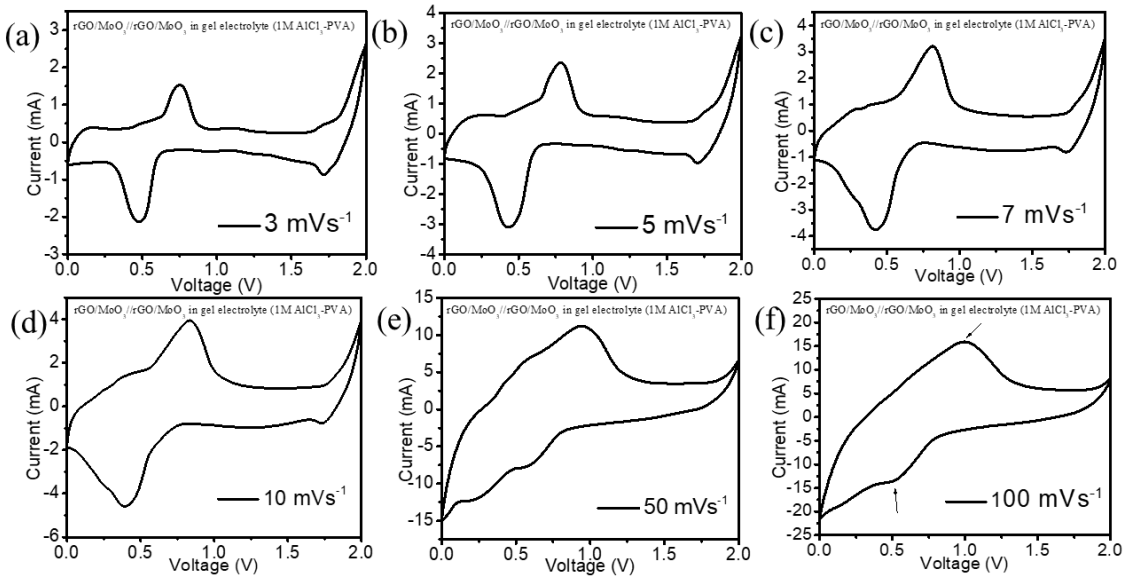

Figure 2.13: CV curves of $rGO/MoO_3//rGO/MoO_3$ cell in the potential range of (0-2) V at scan rate of (a) 3 mVs^{-1}, (b) 5 mVs^{-1}, (c) 7 mVs^{-1}, (d) 10 mVs^{-1}, (e) 50 mVs^{-1} and (f) 100 mVs^{-1} in gel electrolyte (1 M $AlCl_3$-PVA).

It is important to note down here the electrolyte stability. For this purpose, CV experiments were performed at different potential range in a symmetric Ti-Ti cell with 1 M $AlCl_3$ aqueous electrolyte and gel electrolyte (1 M $AlCl_3$-PVA). The reason for choosing Ti is that our previous study indicates that it is an almost inactive current collector [47]. Figure 2.14 shows the CV profiles obtained from Ti-Ti cell in the potential range of (0-1.3) V to (0-2.2) V for 1 M $AlCl_3$ aqueous electrolyte. It could be noticed that there is a sharp rise of current in the positive potential range as the potential window extends from 1.3 V to 2.2 V. This possibly indicates the instability of the electrolyte. However, a comparison of the CV profiles (Figure 2.15(a, b)) of Ti-Ti and $MoO_3//MoO_3$ symmetric cells in 1 M $AlCl_3$ aqueous electrolyte indicates that the redox activity of MoO_3 is considerably higher than the current response obtained from the pristine electrolyte of Ti-Ti cell. Similar effect could also be noticed for the gel electrolyte (1 M $AlCl_3$-PVA) as shown in figure 2.15 (c, d). However, an important point is revealed here. The rise of current could be seen from 1 V onward in case of 1 M $AlCl_3$ aqueous electrolyte (Figure 2.14). Contrarily, this rise is noticed from 1.5 V onward in case of the gel electrolyte (1 M $AlCl_3$-PVA) (Figure 2.16). It indicates that the electrochemical stability of the gel electrolyte (1 M $AlCl_3$-PVA) is better than the 1 M $AlCl_3$ aqueous electrolyte. Overall, it could be fairly assessed that

the redox activity of MoO_3 is not severely affected by the electrolyte instability.

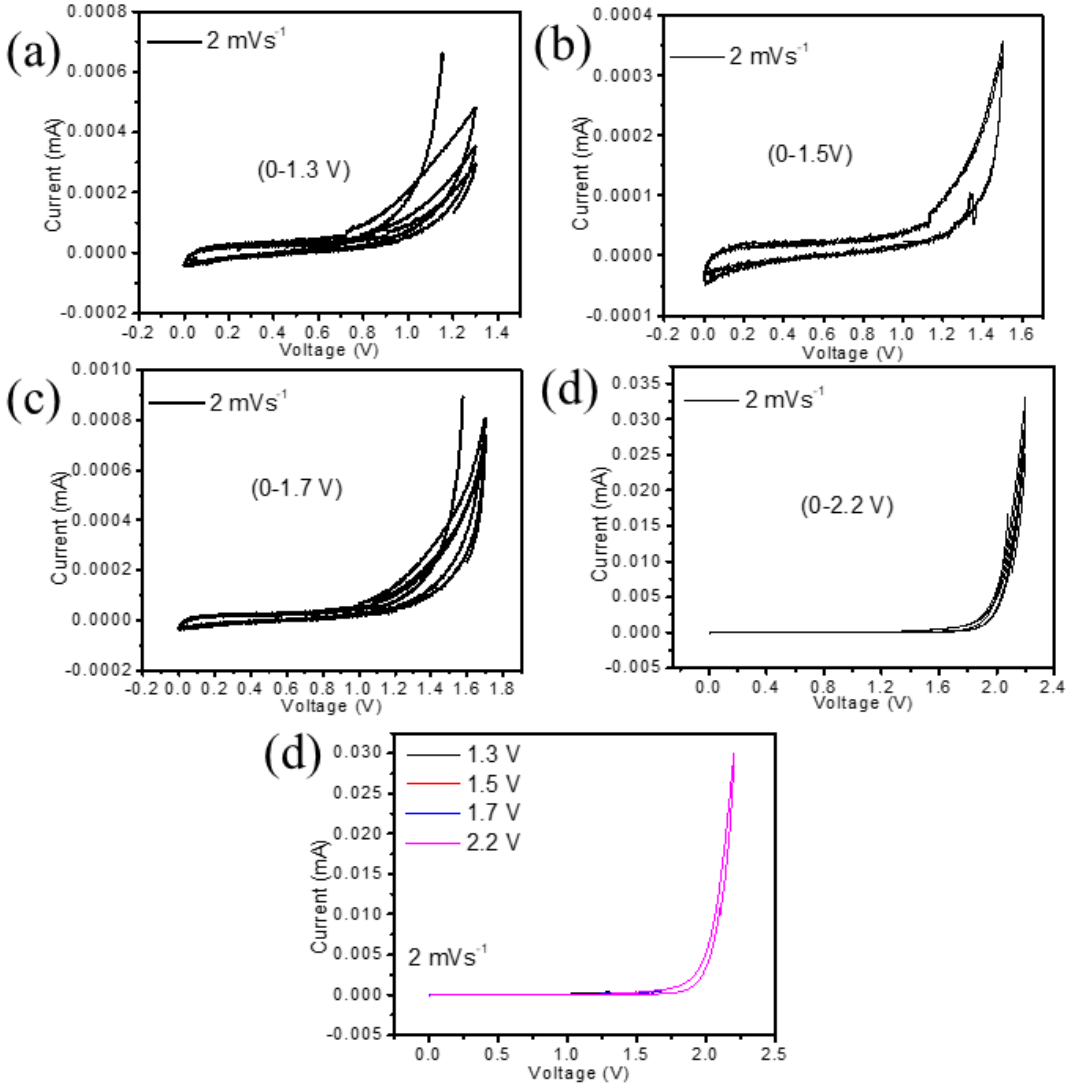

Figure 2.14: Electrolyte stability test. CV curves obtained from a Ti-Ti cell in 1 M $AlCl_3$ aqueous electrolyte at scan rate of 2 mVs^{-1} in the voltage range of (a) (0-1.3) V, (b) (0-1.5) V, (c) (0-1.7) V, (d) (0-2.2) V. (e) comparison of all the CV profiles.

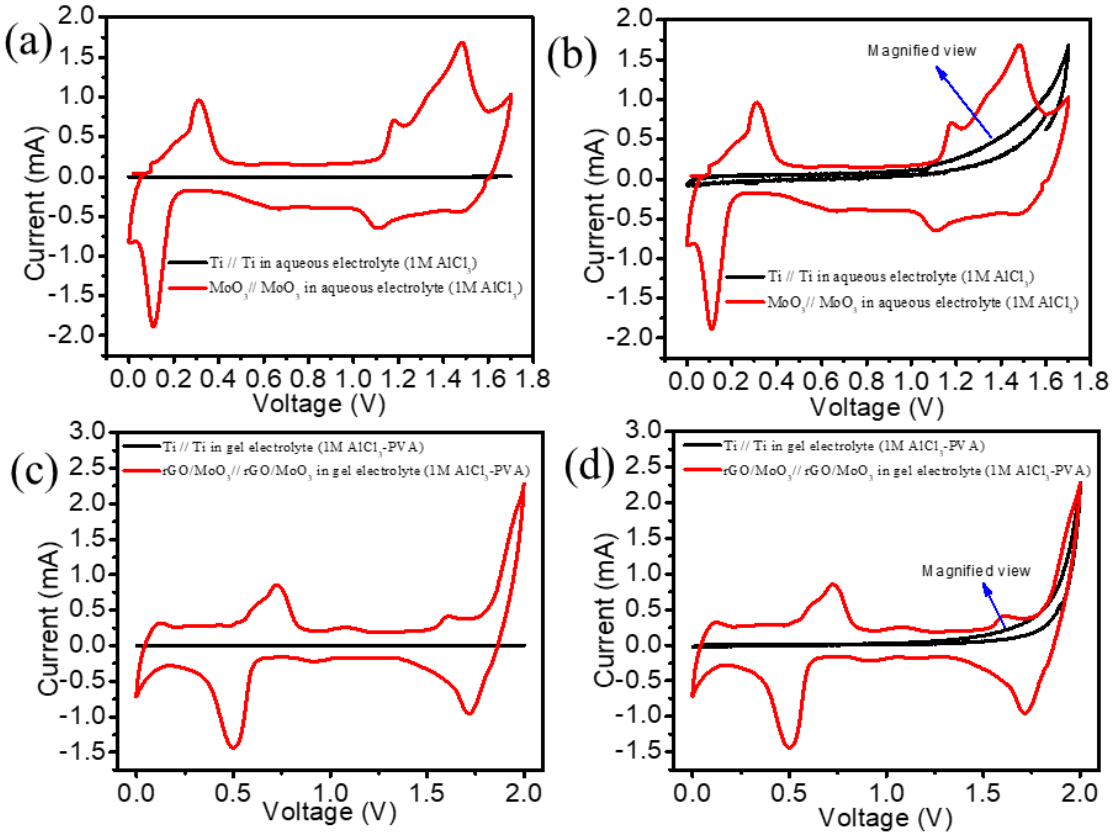

Figure 2.15: Electrolyte stability test. CV curves of (a) Ti-Ti cell and MoO_3//MoO_3 cell in 1 M $AlCl_3$ aqueous electrolyte at scan rate of 2 mVs^{-1}, the magnified version of (a) is shown in (b). CV curves of (c) Ti-Ti cell and rGO/MoO_3//rGO/MoO_3 cell in gel electrolyte (1 M $AlCl_3$-PVA), the magnified version of (c) is shown in (d).

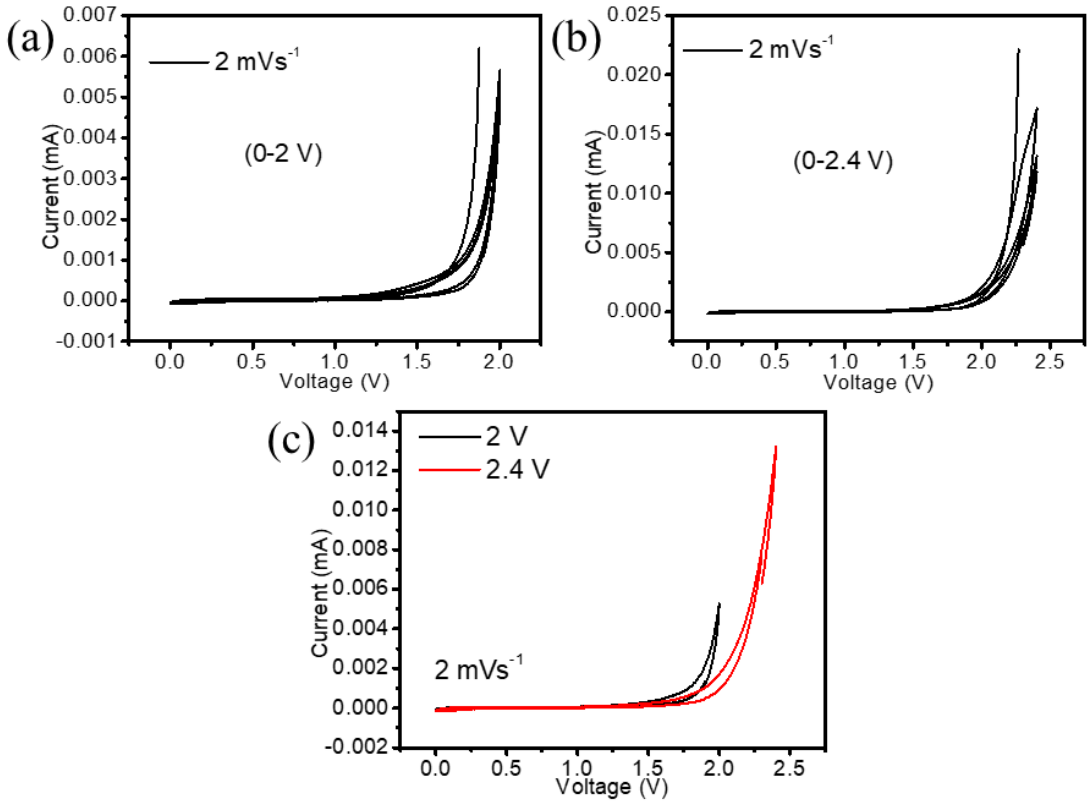

Figure 2.16: Electrolyte stability test. CV curves obtained from a Ti-Ti cell in gel electrolyte (1 M $AlCl_3$-PVA) at scan rate of 2 mVs^{-1} in the voltage range of (a) (0-2) V and (b) (0-2.4) V. (c) comparison of all the CV profiles.

Figure 2.17 shows the galvanostatic charge discharge profiles for MoO_3//MoO_3 and rGO/MoO_3//rGO/MoO_3 symmetric cells at different current densities in 1 M $AlCl_3$ aqueous and gel (1 M $AlCl_3$-PVA) electrolytes. The features in the charge-discharge profiles are in corroboration with the CV profiles. In the case of pristine aqueous electrolyte, a short discharge plateau at 1.15 V and a kink at 0.1 V could be noticed (Figure 2.17a and 2.17b). While during charging, a very short plateau at 0.3 V and a broad plateau at 1.20 V appear. On the other hand, for gel electrolyte, two noticeable discharge plateaus at 1.7 V and 0.5 V could be seen and while charging, two charge plateaus appear at 0.7 V and 1.6 V (Figure 2.17c). The specific capacitance values for the initial cycle of MoO_3//MoO_3 and rGO/MoO_3//rGO/MoO_3 at different current densities for both aqueous and gel electrolytes are given in table 2.1. It is observed that although the charge-discharge and the CV profiles are almost identical for MoO_3//MoO_3 and rGO/MoO_3//rGO/MoO_3 cells, the introduction of rGO resulted in better specific capacitance.

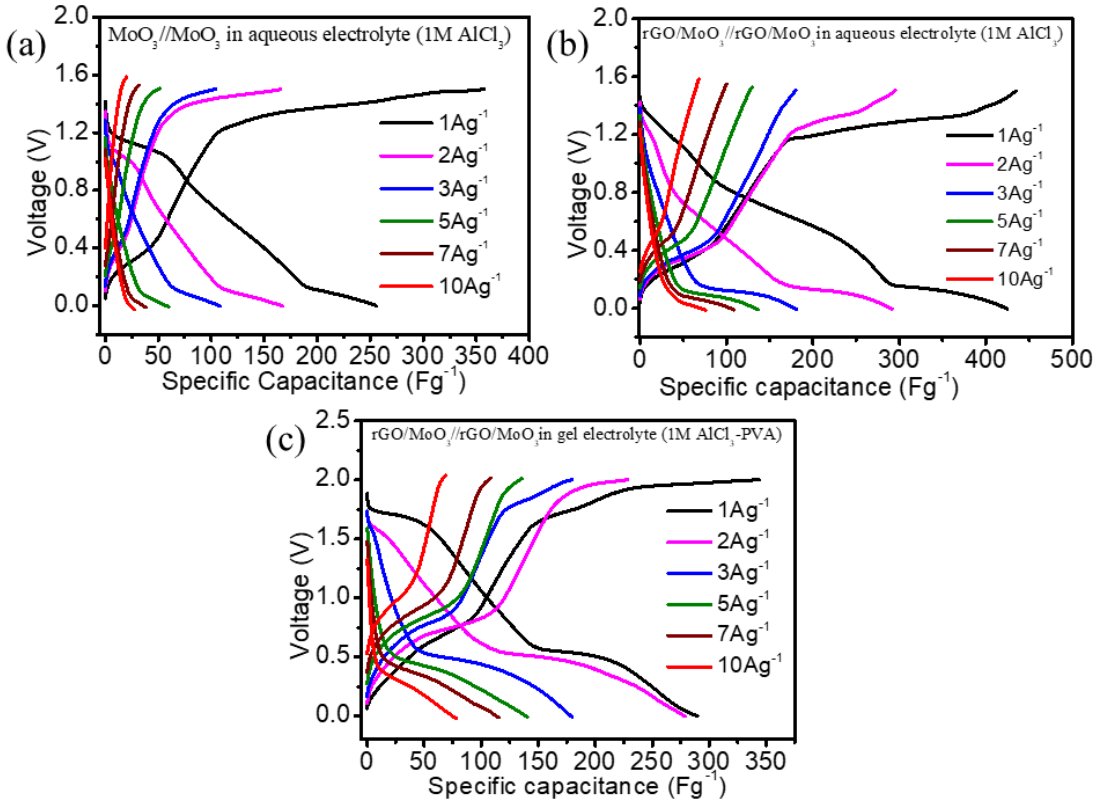

Figure 2.17: Galvanostatic charge-discharge curves of (a) MoO_3//MoO_3 cell in 1 M $AlCl_3$ aqueous electrolyte, (b) rGO/MoO_3//rGO/MoO_3 cell in 1 M $AlCl_3$ aqueous electrolyte and (c) rGO/MoO_3//rGO/MoO_3 in gel electrolyte (1 M $AlCl_3$-PVA).

Table 2.1: Specific capacitance of MoO_3//MoO_3 and rGO/MoO_3//rGO/MoO_3 cells in aqueous and gel electrolytes at different current densities.

Current density (Ag^{-1})	Specific capacitance of MoO_3//MoO_3 in aqueous electrolyte (Fg^{-1})	Specific capacitance of rGO/MoO_3//rGO/MoO_3 in aqueous electrolyte (Fg^{-1})	Specific capacitance of rGO/MoO_3//rGO/MoO_3 in gel electrolyte (Fg^{-1})
1	255	425	290
2	166	290	280
3	106	180	180
5	60	136	141
7	38	108	116
10	28	76	79

Figure 2.18 shows the rate performance of MoO_3//MoO_3 and rGO/MoO_3//rGO/MoO_3 cells as a function of cycle number. The specific capacitance decreases as the current density increases. It could be commented that the cell in gel electrolyte shows better performance since it regains the initial specific capacitance. Figure 2.19a shows the long-term cycle life for MoO_3//MoO_3 and rGO/MoO_3//rGO/MoO_3 cells at current density of 1 Ag^{-1} up to 1000 cycles. The specific capacitance values at 1000^{th} discharge cycle are estimated to be 56 Fg^{-1} and 73 Fg^{-1} for MoO_3//MoO_3 and rGO/MoO_3//rGO/MoO_3 respectively in the pristine aqueous electrolyte, while the same in case of gel electrolyte is 76 Fg^{-1} for rGO/MoO_3//rGO/MoO_3 cell. Figure 2.19b compares the energy density with power density. The energy density and power density values were calculated for the 1^{st} cycle for each current density. The current densities were taken in ascending order i.e. 1 Ag^{-1}, 2 Ag^{-1}, 3 Ag^{-1}, 5 Ag^{-1}, 7 Ag^{-1} and 10 Ag^{-1}. The maximum energy density delivered by MoO_3//MoO_3 and rGO/MoO_3//rGO/MoO_3 cells are about 79 Wh kg^{-1} and 132 Wh kg^{-1} respectively with corresponding power density of 7.5×10^2 W kg^{-1} (at current density of 1 Ag^{-1}) for the aqueous electrolyte. In the case of gel electrolyte, the energy density for rGO/MoO_3//rGO/MoO_3 at current density of 1 Ag^{-1} was estimated to be 161 Wh kg^{-1} corresponding to power density of 10^3 W kg^{-1}. At high current density (10 Ag^{-1}), the energy densities reach to ~ 8 Wh kg^{-1} and ~ 23 Wh kg^{-1} with corresponding power density of 7.5 x 10^3 W kg^{-1} for MoO_3//MoO_3 and rGO/MoO_3//rGO/MoO_3 respectively. In the case of gel electrolyte, the energy density is still ~ 43 Wh kg^{-1} with the corresponding power density of 10^4 W kg^{-1} (at current density of 10 Ag^{-1}) for rGO/MoO_3//rGO/MoO_3. A comparison of the energy and power density with some of the already reported values is shown in table 2.2. It is noted here that these values are not extraordinarily high in the present case, however, this type of study is important for exploration of Al^{3+} ion electrochemical capacitors.

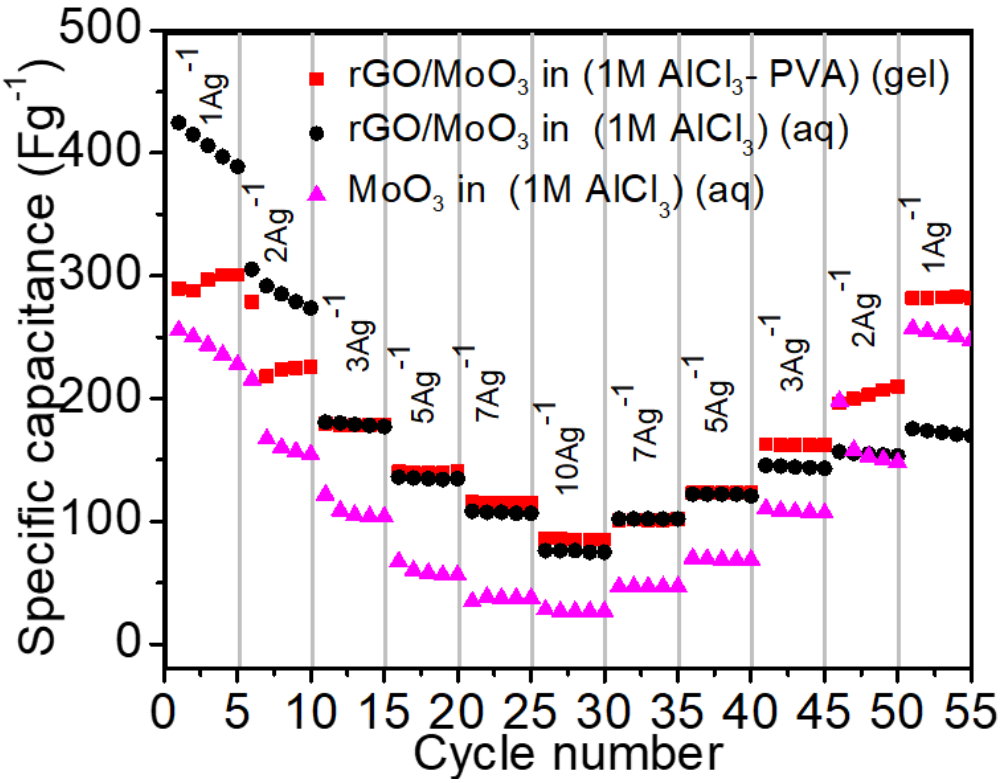

Figure 2.18: Rate performances of MoO_3//MoO_3 and rGO/MoO_3//rGO/MoO_3 cells in aqueous and gel electrolytes.

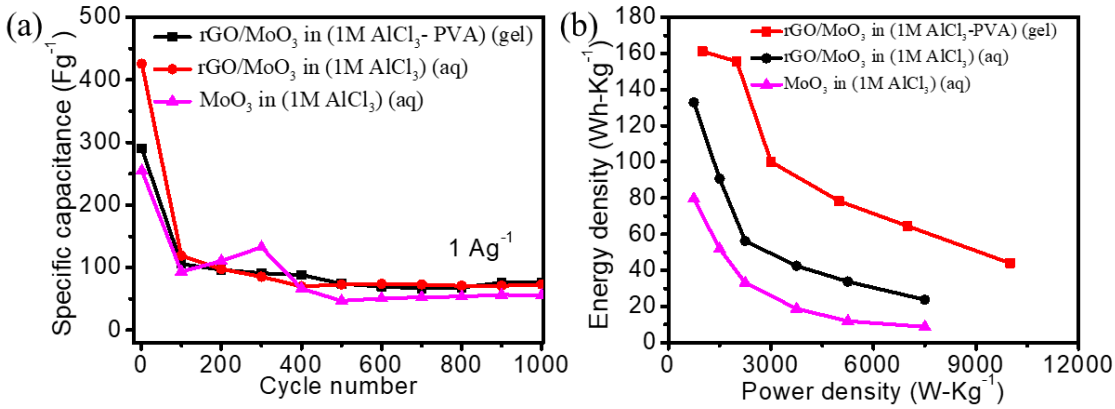

Figure 2.19: (a) Long-term cycle performance at current density of 1 Ag^{-1} up to 1000 cycles and (b) plot of energy density vs power density at different current densities.

Table 2.2: Comparison of energy density and power density of our present work with literature.

Electrode	Electrode configuration	Electrolyte	Potential window (V)	Specific capacitance (Fg^{-1})	Energy density (Wh kg^{-1})	Power density (W kg^{-1})	Reference
AC/MoO_3//AC/MoO_3	Symmetric	1 M Na_2SO_4	1.8	……..	27	225	26
Nio@Ni(OH)$_2$-α- MoO_3// Nio@Ni(OH)$_2$-α-MoO_3	Symmetric	1 M KOH	0.6	……..	24	3100	27
MoO_3// MoO_3	Symmetric	Li_2SO_4	2.0	……..	78	1000	28
MoO_3@CuO// MoO_3@CuO	Symmetric	LiOH/PVA gel	0.8	……..	7.9	8726	29
Mxene/MoO_3// Mxene/MoO_3	Symmetric	1 M H_2SO_4	0.9	……..	13.4	535	30
rGO/MoO_3// rGO/MoO_3	Symmetric	H_2SO_4/PVA gel	1.0	……..	14	500	31
Ag@MoO_3// Ag@MoO_3	Symmetric	1M Na_2SO_4	1.4	……..	15.5	3943	32
MoO_3/Ppy/rGO // MoO_3/Ppy/rGO	Symmetric	1 mol L^{-1} Na_2SO_4	1.2	……..	19.8	301	33
α- MoO_3// α-MoO_3	Symmetric	1M Na_2SO_4	2.2	……..	~ 22	301	34
MoO_3-CNF//MoO_3-CNF	Symmetric	PVA/KOH	1	……..	16.7	340	35
MoO_3// MoO_3	Symmetric	1M $AlCl_3$	1.5	255	79	750	This

rGO/MoO_3// rGO/MoO_3	Symmetric	1M $AlCl_3$	1.5	425	132	750	work
rGO/MoO_3// rGO/MoO_3	Symmetric	1M $AlCl_3$/PVA gel	2.0	290	161	1000	

Another crucial parameter for any energy storage device is the ability to maintain, if not zero, but low self-discharge rate. The self-discharge characteristics for the MoO_3//MoO_3 and rGO/MoO_3//rGO/MoO_3 were also investigated in both the pristine aqueous and gel electrolyte (Figure 2.20). The open circuit potentials of MoO_3//MoO_3 and rGO/MoO_3//rGO/MoO_3 cells in the pristine aqueous electrolyte were measured after charging them up to 1.5 V. In the case of gel electrolyte, the cell was charged up to 2 V. It could be seen that the potential drops to 0.36 V and 0.07 V after 12 h for MoO_3//MoO_3 and rGO/MoO_3//rGO/MoO_3 cells respectively. In contrast, the cell with gel electrolyte exhibits slower rate of self-discharge. The potential drops to only 0.75 V after 21 h (Figure 2.20). It indicates that gel electrolyte may inhibit the self-discharge rate.

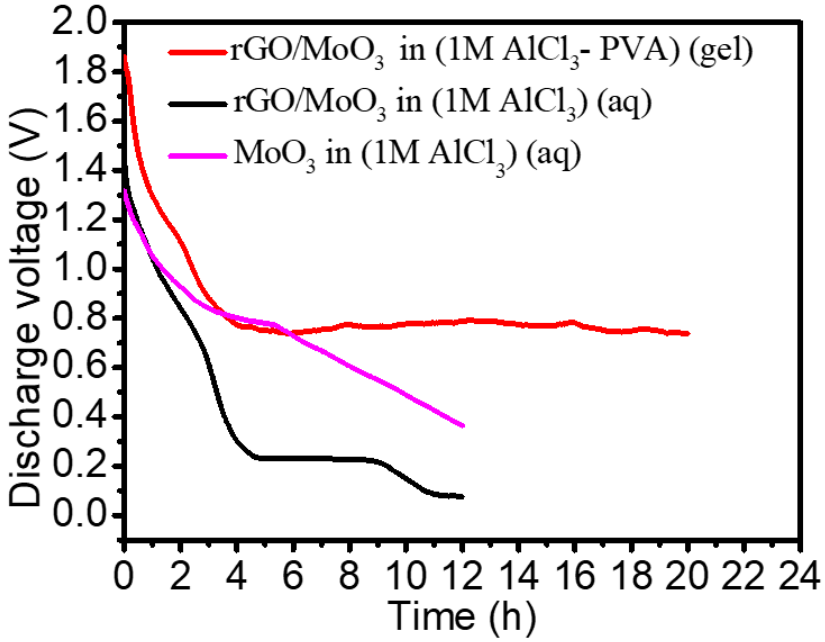

Figure 2.20: self-discharge curves in aqueous and gel electrolytes.

2.4 Conclusion

In summary, an electrochemical investigation for symmetric electrochemical capacitors with MoO_3 nanorod and rGO/ MoO_3 nanorod electrodes is described. The investigation was carried out in aqueous electrolyte (1 M $AlCl_3$) and gel electrolyte (1 M $AlCl_3$-PVA). It is found that the electrochemical behavior of MoO_3 in the gel electrolyte is different than the pristine aqueous electrolyte. For example, there is a shift of the redox peaks and quasi-rectangular feature could not be noticed in the gel electrolyte at high scan rates. The rGO/MoO_3//rGO/MoO_3 cell shows energy and power density of 43 Wh kg^{-1} and 10^4 W kg^{-1} in the gel electrolyte, whereas these values are only 8 Wh kg^{-1} and 7.5 x 10^3 W kg^{-1} for MoO_3//MoO_3 cell in the pristine aqueous electrolyte. In addition, the use of gel electrolyte could significantly reduce self-discharge. The rGO/MoO_3//rGO/MoO_3 cell retains 38 % of charge potential after 21 h in gel electrolyte, while only 5 % could be retained by MoO_3//MoO_3 cell after 12 h in pristine electrolyte.

2.5 References

[1] Sun, J., Luo, B., and Li, H. A review on the conventional capacitors, supercapacitors and emerging hybrid ion capacitors: past, present and future. Adv. Energy *Sustainability Res*., 3: 2100191, 2022.

[2] Zhao, C., and Zheng, W. A review for aqueous electrochemical capacitors. *Front. Energy Res*., 3: 23, 2015.

[3] Kotz, R., and Carlen, M. Principles and applications of electrochemical capacitors. *Electrochim. Acta*, 45: 2483-2498, 2000.

[4] Aravindan, V., Gnanaraj, J., Lee, Y.S., and Madhavi, S. Insertion type electrodes for nonaqueous Li-ion capacitors. *Chem. Rev*., 114: 11619-11635, 2014.

[5] Yan, J., Li, S., Lan, B., Wu, Y., and Lee, P.S. Rational design of nanostructured electrode materials towards multifunctional supercapacitors. *Adv. Func. Mater*., 30: 1902564, 2019.

[6] Huang, Y., Zhong, M., Huang, Y., Zhu, M., Pei, Z., Wang, Z., Xue, Q., Xie, X., and Zhi, C. A self-healable and highly stretchable supercapacitors based on a dual cross linked polyelectrolyte. *Nat. Commun*., 6: 10310, 2015.

[7] Huang, C., Zhang, J., Young, N.P., Snaith, H.J., and Grant, P.S. Solid-state supercapacitors with rationally designed heterogeneous electrodes fabricated by

large area spray processing for wearable energy storage applications. *Sci*. *Rep*., 6:25684, 2016.

[8] Amatucci, G.G., Badway, F., Du, P.A., and Zheng, T. An asymmetric hybrid nonaqueous energy storage cell. *J*. *Electrochem*. *Soc*., 148: A930, 2001.

[9] Dong, L., Yang, W., Yang, W., Li, Y., Wu, W., and Wang, G. Multivalent metal ion hybrid capacitors: a review with a focus on zinc-ion hybrid capacitors. *J*. *Mater*. *Chem*. *A*, 7: 13810-13832, 2019.

[10] Thalji, M.R., Ali, G.A.M., Algarni, H., and Chong, K.F. Al^{3+}ion intercalation pseudocapacitance study of $W_{18}O_{49}$ nanostructure. *J. Power Sources*, 438: 227028, 2019.

[11] Li, K., Shao, Y., Liu, S., Zhang, Q., Wang, H., Li, Y., and Kaner, R.B. Aluminum-ion-intercalation supercapacitors with ultrahigh areal capacitance and highly enhanced cycling stability: power supply for flexible electrochromic devices. *Small*, 13: 1700380, 2017.

[12] Ma, H., Chen, H., Hu, Y., Yang, B., Feng, J., Xu, Y., Sun, Y., Cheng, H., Li, C., Yan, X., and Qu, L. Aqueous rocking-chair aluminium-ion capacitors enabled by self-adaptive electrochemical pore-structure remolding approach. *Energy Environ Sci*., 15: 1131-1143, 2022.

[13] Cheng, X., Pan, J., Zhao, Y., Liao, M., and Peng, H. Gel polymer electrolytes for electrochemical energy storage. *Adv*. *Energy Mater*., 8: 1702184, 2017.

[14] Dai, H., Zhang, G., Rawach, D., Fu, C., Wang, C., Liu, X., Dubois, M., Lai, C., and Sun, S. Polymer gel electrolytes for flexible supercapacitors: Recent progress, challenges and perspective. *Energy Storage Mater*., 34: 320-355, 2020.

[15] Alipoori, S., Mazinani, S., Aboutalebi, S.H., and Sharif, F. Review of PVA-based gel polymer electrolytes in flexible solid-state supercapacitors: Opportunities and challenges. *J. Energy Storage*, 27: 101072, 2020.

[16] Latoszynska, A.A., Zukowska, G.Z., Rutkowska, I.A., Taberna, P.L., Simon, P., Kulesza, P.J. and Wieczorek, W. Non-aqueous gel polymer electrolyte with phosphoric acid ester and its application for quasi solid-state supercapacitors. *J. Power Sources*, 274: 1147-1154, 2015.

[17] Thanh, H.T.T., Le, P.A., Thi, M.D., Le, Q.T., and Trinh, T.N. Effect of gel polymer electrolyte based on polyvinyl/alcohol/polyethylene oxide blend and sodium salts on the performance of solid-state supercapacitor. *Bull*. *Mater*. *Sci*., 41: 145, 2018.

[18] Gong, Y., Dong, Y., Zhao, B., Yu, R., Hu, S., and Tan, Z. Diverse application of MoO_3 for high performance organic photovoltaics: fundamentals, processes and optimization. *J. Mater. Chem*. A, 8: 978-1009, 2020.

[19] Yu, M., Shao, H., Wang, G., Yang, F., Liang, C., Rozire, P., Wang, C.Z., Lu, X., Simon, P., and Feng, X. Interlayer gap widened α-phase molybdenum trioxide as high-rate anodes for dual-ion intercalation energy storage devices. *Nat. Commun.*, 11: 1348, 2020.

[20] Malik, R., Joshi, N., and Tomer, V.K. Advances in the designs and mechanisms of MoO_3 nanostructures for gas sensors: a holistic review. *Mater. Adv.* 2: 4190-4227, 2021.

[21] Zhu, Y., Yao, Y., Luo, Z., Pan, C., Yang, J., Fang, Y., Deng, H., Liu, C., Tan, Q., Liu, F., and Guo, Y. Nanostructured MoO_3 for efficient energy and environmental catalysis. *Molecules*, 25: 18, 2020.

[22] Dai, H., Wang, L., Zhao, Y., Xue, J., Zhou, R., Yu, C., An, J., Zhou, J., Chen, Q., Sun, G., and Huang, W. Recent advances in molybdenum-based materials for lithium sulfur batteries. *Research*, 2021.

[23] Zhou, L., Yang, L., Yuan, P., Zou, J., Wu, Y., and Yu, C. α-MoO_3 nanobelts: A high performance cathode material for lithium ion batteries. *J. Phys. Chem. C*, 114: 21868-21872, 2010.

[24] Chen, J.S., Cheah, Y.L., Madhavi, S., and Lou, X.W. Fast synthesis of α-MoO_3 nanorods with controlled aspect ratios and their enhanced lithium storage capabilities. *J. Phys. Chem. C*, 114: 8675-8678, 2010.

[25] Freitas, A.P., Andre, R.F., Poucin, C., Li, T.K.C., Imbao, J., Kaiser, B.L., and Carenco, S. Guidelines for the molybdenum oxidation state and geometry from X-ray absorption spectroscopy at the Mo $L_{2,3}$-edges. *J. Phys. Chem. C*, 125: 17761-17773, 2021.

[26] Sangeetha, D.N., Bhat, D.K., and Selvakumar, M. h-MoO_3/Activated carbon nanocomposites for electrochemical applications. *Ionics*, 25: 607-616, 2019.

[27] Manibalan, G., Govindaraj, Y., Yesuraj, J., Kuppusami, P., Murugadoss, G., Murugavel, R., and Kuma, M.R. Facile synthesis of NiO@$Ni(OH)_2$-α-MoO_3 nanocomposite for enhanced solid state symmetric supercapacitor application. *J. Coll. Int. Sci.*, 585: 505-518, 2020.

[28] Zhao, N., Fan, H., Zhang, M., Ma, J., Du, Z., Yan, B., Li, H., and Jiang, X. Simple electrodeposition of MoO_3 film on carbon cloth for high-performance

aqueous symmetric supercapacitors. *Chemical Engineering Journal*, 390: 124477, 2020.

[29] Zhang, Y., Lin, B., Wang, J., Han, P., Xu, T., Sun, Y., Zhang, X., and Yang, H. Polyoxometalates@metal-organic frameworks derived porous MoO_3@CuO as electrodes for symmetric all-solid-state supercapacitor. *Electrochim. Acta*, 191: 795-804, 2016.

[30] Wang, Y., Wang, X., Li, X., Liu, R., Bai, Y., Xiao, H., Liu, Y., and Yuan, G. Intercalating ultrathin MoO_3 nanobelts into MXene film with ultrahigh volumetric capacitance and excellent deformation for high energy density devices. *Nano-micro Lett.*,12: 115, 2020.

[31] Cao, X., Zheng, B., Shi, W., Yang, J., Fan, Z., Luo, Z., Rui, X., Chen, B., Yan, Q., and Zhang, H. Reduced graphene oxide wrapped MoO_3 composites prepared by using metal organic frameworks as precursor for all solid state flexible supercapacitors. *Adv. Mater.*, 27: 4695-4701, 2015.

[32] Zhou, C., Wang, Q., Yan, X.H., Wang, J.J., Wang, D.F., Yuan, X.X., Jiang, H., Zhu, Y.H., and Cheng, X.N. A facile route to synthesize Ag decorated MoO_3 nanocomposite for symmetric supercapacitor. *Ceram. Int*., 46: 15385-15391, 2020.

[33] Deng, H., Huang, J., Hu, Z., Chen, X., Huang, D., and Jin, T. Fabrication of a three-dimensionally networked MoO_3/PPy/rGO composite for a high-performance symmetric supercapacitor. *ACS Omega,* 6: 9426-9432, 2021.

[34] Elkholy, A.E., Duignan, T.T., Sun, X., and Zhao, X.S. Stable α-MoO_3 electrode with a widened electrochemical potential window for aqueous electrochemical capacitors. *ACS Appl. Energy Matter.*, 4: 3210-3220, 2021.

[35] Tian, K., Wei, Lu., Zhang, X., Jin, Y., and Guo, X. Membranes of carbon nanofibers with embedded MoO_3 nanoparticles showing superior cycling performance for all solid state flexible supercapacitors. *Mater. Today Energy*, 6: 27-35, 2017.

[36] Lahan, H., and Das, S.K. Al^{3+} ion intercalation in MoO_3 for aqueous Al ion battery. *J. Power Sources*, 413: 134-138, 2019.

[37] Wang, F., Liu, Z., Wang, X., Yuan, X., Wu, X., Zhu, Y., Fu, L., and Wu, Y. A conductive polymer coated MoO_3 anode enables an Al-ion capacitor with high performance. *J. Mater. Chem. A*, 4: 5115-5123, 2016.

[38] Li, S., Shao, C., Liu, Y., Tang, S., and Mu, R. Nanofibers and nanoplatelets of MoO_3 via an electrospinning technique. *J. Phys. Chem. Solids*, 67: 1869-1872, 2006.

[39] Sajjad, M., Khan, M.I., Cheng, F., and Lu, W. A review on selection criteria of aqueous electrolytes performance evaluation for advanced asymmetric supercapacitors. *J. Energy Storage*, 40: 102729, 2021.

[40] Murugan, R., and Chang, H. Thermo-Raman investigations on thermal decomposition of $(NH_4)_6Mo_7O_{24}$.$4H_2O$. *J. Chem. Soc., Dalton Trans*. 3125-3132, 2001.

[41] Ma, E. The thermal decomposition of ammonium polymolybdates. *Bull. Chem. Soc. Jpn.* 37: 171, 1964.

[42] Shahriary, L., and Athawale, A., Graphene oxide synthesized by using Modified Hummers approach. *Int. J. Renew. Energy Environ. Eng.*, 2: 2348-0157, 2014.

[43] Hashem, A.M., Groult, H., Mauger, A., Zaghib, K., and Julien, C.M. Electrochemical properties of nanofibers α-MoO_3 as cathode materials for Li batteries. *J. Power Source*, 219: 126-132, 2012.

[44] Iriyama, Y., Abe, T., Inaba, M., and Ogumi, Z. Transmission electron microscopy (TEM) analysis of two-phase reaction in electrochemical lithium insertion within α-MoO_3. *Solid State Ion.* 135: 95-100, 2000.

[45] Li, W., Cheng, F., Tao, Z., and Chen, J. Vapor-transportation preparation and reversible lithium intercalation / deintercalation of α-MoO_3 microrods. *J. Phys. Chem. B*, 110: 119-124, 2006.

[46] Sanchez, B.M., and Grant, P.S. Charge storage properties of a α-MoO_3/carboxyl-functionalized single-walled carbon nanotube composite electrode in a Li ion electrolyte. *Electrochem. Acta*, 98: 294-302, 2013.

[47] Lahan, H., and Das, S.K. Active role of inactive current collector in aqueous aluminum-ion battery. *Ionics*, 24: 2175-2180, 2018.